



## Plasma-assisted stabilization of laminar premixed methane/air flames around the lean flammability limit

Moon Soo Bak<sup>a,\*</sup>, Hyungrok Do<sup>b</sup>, Mark Godfrey Mungal<sup>a,c</sup>, Mark A. Cappelli<sup>a</sup>

<sup>a</sup> Mechanical Engineering Department, Stanford University, Stanford, CA 94305-3032, United States

<sup>b</sup> Aerospace & Mechanical Engineering, University of Notre Dame, Notre Dame, IN 46556, United States

<sup>c</sup> School of Engineering, Santa Clara University, Santa Clara, CA 95053, United States

### ARTICLE INFO

#### Article history:

Received 8 November 2011

Received in revised form 16 February 2012

Accepted 30 March 2012

Available online 24 April 2012

#### Keywords:

Plasma-assisted combustion

Pulsed discharges

Lean flammability limit

### ABSTRACT

Studies of nanosecond repetitively pulsed discharge plasma-assisted combustion were carried out on a laminar premixed methane/air flow in the vicinity of the lean flammability limit. Experimental results indicated that complete combustion is achieved when the equivalence ratio is above the known lean flammability limit ( $\phi = 0.53$ ) at high discharge repetition rates of 50 kHz. When the ratio is below the limit, the plasma does serve as a flame holder; however, only partial combustion is seen in the downstream flow. Two-dimensional kinetic simulation results were found to be consistent with the experimental results. The simulations revealed that the methane is fully consumed within the discharge region, since the time between discharge pulses is less than that for species diffusion and advection. This creates a source of radicals and high temperature, which diffuse outwards to stabilize the combustion of the surrounding flow.

© 2012 The Combustion Institute. Published by Elsevier Inc. All rights reserved.

### 1. Introduction

Nanosecond repetitive pulsed discharges have been shown to be an effective method of stabilizing the combustion of premixed lean fuel/air mixtures [1–9]. The stabilization is attributed to the production of active radicals and gas heating [1,3,4]. Previous work has focused largely on investigating the kinetics responsible for enhancing combustion, and less have focused on the propagation of this combustion towards surrounding flows. Some studies [1,5] use either OH or CH chemiluminescence as an indicator of combustion below the lean flammability limit, however, such measurements should be interpreted with caution since radicals can be produced from the discharge by collisional quenching of electronically excited species (e.g.  $N_2$ ). One study [6] has carried out gas-chromatography which confirms directly that combustion has produced product species, even at very low equivalence ratios, well below the lean flammability limit. They reported the extension in the lean flammability limit of premixed methane–air, but the mixtures are preheated and the deposited power into the plasma source is significant when compared to the combustion power itself.

Kinetic simulations [7–9] have also been used to study the detailed chemistry in nanosecond pulsed discharges. Most of these

simulations are zero-dimensional [7–9] (i.e., do not include any spatial dimensions) and are intended to validate the experiments conducted at low temperature (about 300 K) and low pressures (up to a few tens of torr). Higher dimensional simulations that account for the repetitive nature of the discharge are rare, since practical combustion occurs at high pressure (at least above atmospheric pressure) and in these conditions discharges tend to be more filamentary [10] (highly multi-dimensional). Clearly, one or two-dimensional (1-D or 2-D) discharge simulations must account for the effects of diffusion and advection as well as the effect that the repetitive discharge has on the evolution of the discharge chemistry.

In this work, we have carried out measurements of stable species formed in methane/air combustion downstream of the plasma source by gas-chromatography and gas temperatures either through the use of thermocouples or optical emission spectroscopy of the electronically excited nitrogen ( $N_2$ ) C–B transition. 2-D simulations are also conducted to investigate the interaction between the discharge and surrounding methane/air mixture as well as the detailed kinetics within the discharge.

### 2. Experimental setup

A schematic of the experimental setup is shown in Fig. 1. Nanosecond pulsed discharge plasmas were generated between two tungsten electrodes (1 mm diameter, 1 mm separation) using a pulse generator (FID Technology F1112). The horizontally-oriented

\* Corresponding author. Address: Bldg. 520, Duena Street, Stanford, CA 94305-3032, United States. Fax: +1 650 723 1748.

E-mail address: [moonsoo@stanford.edu](mailto:moonsoo@stanford.edu) (M.S. Bak).

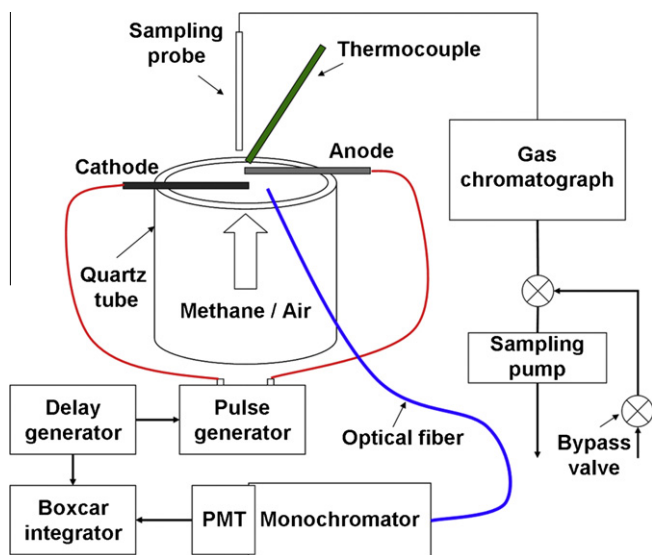


Fig. 1. Schematic of experimental setup for gas-chromatographic and optical emission measurements.

electrodes were displaced vertically to generate vertically oriented discharges and so minimize the effect of an ionic wind on flow and combustion. The pulse generator generated a near-Gaussian temporal voltage pulse of 8 kV peak and 9 ns full width at half maximum (FWHM) at repetition rates between 10 and 50 kHz. Methane and air were first premixed in a plenum and then discharged into a quartz tube of 44 mm inner diameter. The bottom electrode was placed 1 mm above from the confined flow exiting this tube, thereby minimizing the effects of air entrainment. The total flow rate and their ratios were maintained using digital mass flow controllers (Unit UFC-3020A for air and MKS 247C for methane). The flow speed was about 42.5 cm/s.

Plasma-induced combustion products were analyzed using a gas-chromatograph (GC) (Varian, Inc.) equipped with Porapak Q and Molsieve 5 Å columns, and a thermal conductivity detector (TCD, with a resolution of below 1% in mole fraction) and pulsed discharge helium ionization detector (PDHID, with a resolution of below 100 ppm in mole fraction).  $H_2$ , Air,  $CH_4$ , CO, and  $CO_2$  were separated via the Porapak Q, and the separation of  $N_2$  and  $O_2$  was achieved via the Molsieve 5 Å. A quartz sampling probe (1.8 mm inner diameter) was placed at between 3 mm and 11 mm downstream of the discharge. A sampling pump (Thermo Scientific 420-1901) equipped with a bypass valve was attached to the end of a sampling loop to draw samples into the gas-chromatograph. Since water is not allowed in the Molsieve 5 Å, the samples were directed to flow through a desiccant (Drierite) before entering the GC. The bypass valve was adjusted to match the suction speed at the probe tip to the flow speed. The sampling time was set to be enough to refresh the remaining gas from the previous measurements. This refreshing was confirmed through the sampling of a stream of pure nitrogen. Gas temperatures were also measured at the sampling locations using a 0.13 mm S-type thermocouple (Omega Engineering, Inc.). Thermocouple data are corrected for radiation [11], but not for other effects such as heat conduction along the wire and catalytic effects on the wire surface.

The spectrally-resolved emission associated with the electronically excited  $N_2$  C–B transition was also measured to extract rotational and vibrational temperatures. Light emitted from the center of the discharge was collected and transmitted by an optical fiber to a monochromator (Jarrell-Ash 82-020). The light was dispersed by the monochromator and recorded by a photomultiplier (PMT) designed for fast-time response (Hamamatsu R928 with

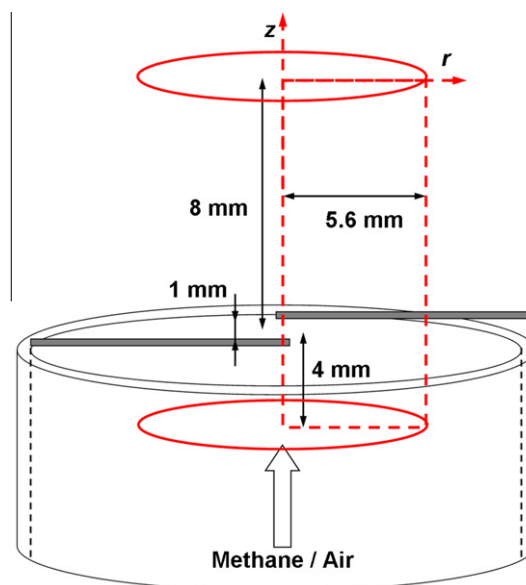


Fig. 2. 2-D kinetic simulation domain.

Hamamatsu E717-63 socket). The PMT signal was then gated, integrated, and averaged using a boxcar integrator (SRS SR250) with 2 ns gate width, synchronized to the pulse generator using a delay generator (SRS DG535).

### 3. Simulation

2-D kinetic simulations of the plasma-induced combustion have been developed to investigate the detailed chemistry that takes place within the discharge and the transport of the resulting species/energy to its immediate surroundings. The simulated domain is shown in Fig. 2, marked as a red<sup>1</sup> dotted box. Axisymmetric coordinates are used and the size of the domain is set to 12 mm in height ( $z$ -axis) and 5.6 mm in radius ( $r$ -axis), spanning the discharge region. The center of the discharge region is located at a position 4 mm above from the lower computational boundary, on the axis, and has size of 1 mm in height and 0.35 mm in diameter. This diameter is chosen to agree with the measured diameter in the similar experiments of Pai et al. [10]. A uniform grid spacing (0.333 mm along the  $z$ -axis and 0.175 mm along the  $r$ -axis) is used in these simulations. Species considered include ground and electronic excited states of  $N_2$  (X, A, B, a', C), the ground electronic states of  $O_2$ ,  $N_2^+$ ,  $O_2^+$ , O,  $CH_4$ ,  $H_2O$ ,  $CO_2$ ,  $CH_4^+$ ,  $H_2O^+$ ,  $CO_2^+$ , and free electrons (e), amongst others. These species are included in a reduced reaction mechanism, DRM19 [12], for methane/air combustion. DRM19 has been tested against the more detailed GRI-Mech [13] mechanism for computing ignition delay times and laminar flame speeds. Thermodynamic properties for neutral species are calculated based on the use of NASA polynomials as tabulated in the GRI-Mech package. The thermodynamic properties for electrons and ions are taken from Burcat [14]. Reactions considered are electron-impact excitation and ionization of  $N_2$ , electron-impact dissociation and ionization of  $O_2$  and  $CH_4$ , electron-impact ionization of  $H_2O$  and  $CO_2$ , ion conversion, recombination of electron and positive ions, quenching of electronically excited nitrogen ( $N_2^*$ ) by  $N_2$ , dissociative quenching of  $N_2^*$  by  $O_2$  and  $CH_4$ , and chemical transformation of neutral species typical in methane/air combustion reaction mechanisms. The reactions pertinent to the plasma kinetics and associated rates are provided in Table 1. Rate coefficients for

<sup>1</sup> For interpretation of color in Figs. 1–12, the reader is referred to the web version of this article.

**Table 1**  
Reaction set (except the DRM19 reduced methane/air combustion mechanism) used in 2-D kinetic simulations for methane/air plasma-induced combustion.

Reaction	Rate coefficient	Reference
$N_2 + e \rightarrow N_2(A) + e$	$\sigma$	[26]
$N_2 + e \rightarrow N_2(B) + e$	$\sigma$	[26]
$N_2 + e \rightarrow N_2(a') + e$	$\sigma$	[26]
$N_2 + e \rightarrow N_2(C) + e$	$\sigma$	[26]
$N_2 + e \rightarrow N_2^+ + 2e$	$\sigma$	[26]
$O_2 + e \rightarrow 2O + e$	$\sigma$	[27]
$O_2 + e \rightarrow O_2^+ + 2e$	$\sigma$	[27]
$CH_4 + e \rightarrow CH_3 + H + e$	$\sigma$	[28]
$CH_4 + e \rightarrow CH_4^+ + 2e$	$\sigma$	[28]
$H_2O + e \rightarrow H_2O^+ + 2e$	$\sigma$	[28]
$CO_2 + e \rightarrow CO_2^+ + 2e$	$\sigma$	[28]
$O_2^+ + e \rightarrow 2O$	$2 \times 10^{-7} (300/T_e)^{0.63} \text{ cm}^3/\text{s}$	[16]
$CH_4^+ + e \rightarrow CH_3 + H$	$2.9 \times 10^{-7} (300/T_e)^{0.53} \text{ cm}^3/\text{s}$	[17]
$H_2O^+ + e \rightarrow O + 2H$	$10^{-6} (300/T_e)^{0.5} \text{ cm}^3/\text{s}$	[18]
$CO_2^+ + e \rightarrow O + CO$	$4 \times 10^{-7} (300/T_e)^{0.5} \text{ cm}^3/\text{s}$	[19]
$e + e + N_2^+ \rightarrow e + N_2$	$10^{-19} (300/T_e)^{4.5} \text{ cm}^6/\text{s}$	[16]
$e + N_2^+ + N_2 \rightarrow N_2 + N_2$	$6 \times 10^{-27} (300/T_e)^{1.5} \text{ cm}^6/\text{s}$	[16]
$e + N_2^+ + O_2 \rightarrow N_2 + O_2$	$6 \times 10^{-27} (300/T_e)^{1.5} \text{ cm}^6/\text{s}$	[16]
$e + e + O_2^+ \rightarrow e + O_2$	$10^{-19} (300/T_e)^{4.5} \text{ cm}^6/\text{s}$	[16]
$e + O_2^+ + N_2 \rightarrow O_2 + N_2$	$6 \times 10^{-27} (300/T_e)^{1.5} \text{ cm}^6/\text{s}$	[16]
$e + O_2^+ + O_2 \rightarrow O_2 + O_2$	$6 \times 10^{-27} (300/T_e)^{1.5} \text{ cm}^6/\text{s}$	[16]
$e + e + H_2O^+ \rightarrow e + H_2O$	$10^{-19} (300/T_e)^{4.5} \text{ cm}^6/\text{s}$	<sup>a</sup>
$e + H_2O^+ + N_2 \rightarrow H_2O + N_2$	$6 \times 10^{-27} (300/T_e)^{1.5} \text{ cm}^6/\text{s}$	<sup>a</sup>
$e + H_2O^+ + O_2 \rightarrow H_2O + O_2$	$6 \times 10^{-27} (300/T_e)^{1.5} \text{ cm}^6/\text{s}$	<sup>a</sup>
$e + e + CO_2^+ \rightarrow e + CO_2$	$10^{-19} (300/T_e)^{4.5} \text{ cm}^6/\text{s}$	<sup>a</sup>
$e + CO_2^+ + N_2 \rightarrow CO_2 + N_2$	$6 \times 10^{-27} (300/T_e)^{1.5} \text{ cm}^6/\text{s}$	<sup>a</sup>
$e + CO_2^+ + O_2 \rightarrow CO_2 + O_2$	$6 \times 10^{-27} (300/T_e)^{1.5} \text{ cm}^6/\text{s}$	<sup>a</sup>
$N_2^+ + O_2 \rightarrow O_2^+ + N_2$	$6 \times 10^{-11} (300/T_g)^{0.5} \text{ cm}^3/\text{s}$	[15]
$N_2^+ + H_2O \rightarrow H_2O^+ + N_2$	$2.3 \times 10^{-9} \text{ cm}^3/\text{s}$	[15]
$H_2O^+ + O_2 \rightarrow O_2^+ + H_2O$	$4.3 \times 10^{-10} \text{ cm}^3/\text{s}$	[15]
$CO_2^+ + O_2 \rightarrow O_2^+ + CO_2$	$5.6 \times 10^{-11} \text{ cm}^3/\text{s}$	[20]
$N_2(A) + N_2 \rightarrow N_2 + N_2$	$3 \times 10^{-16} \text{ cm}^3/\text{s}$	[15]
$N_2(B) + N_2 \rightarrow N_2 + N_2$	$2 \times 10^{-12} \text{ cm}^3/\text{s}$	[15]
$N_2(B) + N_2 \rightarrow N_2(A) + N_2$	$3 \times 10^{-11} \text{ cm}^3/\text{s}$	[15]
$N_2(B) \rightarrow N_2(A) + h\nu$	$1.5 \times 10^5 \text{ 1/s}$	[15]
$N_2(a') + N_2 \rightarrow N_2(B) + N_2$	$1.9 \times 10^{-13} \text{ cm}^3/\text{s}$	[15]
$N_2(C) + N_2 \rightarrow N_2(a') + N_2$	$10^{-11} \text{ cm}^3/\text{s}$	[15]
$N_2(C) \rightarrow N_2(B) + h\nu$	$3 \times 10^7 \text{ 1/s}$	[15]
$N_2(A) + N_2(A) \rightarrow N_2(B) + N_2$	$3 \times 10^{-10} \text{ cm}^3/\text{s}$	[15]
$N_2(A) + N_2(A) \rightarrow N_2(C) + N_2$	$1.5 \times 10^{-10} \text{ cm}^3/\text{s}$	[15]
$N_2(A) + O_2 \rightarrow N_2 + 2O$	$2.3 \times 10^{-12} \text{ cm}^3/\text{s}$	[15]
$N_2(B) + O_2 \rightarrow N_2 + 2O$	$2 \times 10^{-10} \text{ cm}^3/\text{s}$	[15]
$N_2(a') + O_2 \rightarrow N_2 + 2O$	$2.8 \times 10^{-11} \text{ cm}^3/\text{s}$	[15]
$N_2(C) + O_2 \rightarrow N_2 + 2O$	$3 \times 10^{-10} \text{ cm}^3/\text{s}$	[15]
$N_2(A) + O \rightarrow N_2 + O$	$2.1 \times 10^{-11} \text{ cm}^3/\text{s}$	[15]
$O + O + N_2 \rightarrow O_2 + N_2$	$10^{-33} (300/T_g)^{0.41} \text{ cm}^6/\text{s}$	[15]
$O + O + O_2 \rightarrow O_2 + O_2$	$4 \times 10^{-33} (300/T_g)^{0.41} \text{ cm}^6/\text{s}$	[15]
$CH_4 + N_2(A) \rightarrow CH_3 + H + N_2$	$3.3 \times 10^{-15} \text{ cm}^3/\text{s}$	[21]
$CH_4 + N_2(B) \rightarrow CH_3 + H + N_2$	$3 \times 10^{-10} \text{ cm}^3/\text{s}$	[22]
$CH_4 + N_2(a') \rightarrow CH_3 + H + N_2$	$3 \times 10^{-10} \text{ cm}^3/\text{s}$	[23]
$CH_4 + N_2(C) \rightarrow CH_3 + H + N_2$	$5 \times 10^{-10} \text{ cm}^3/\text{s}$	[24]

<sup>a</sup> This rate coefficient is estimated based on Ref. [16].

reactions between neutral species and ions are adapted from the previous literature [15–24], whereas those for reactions involving electrons are calculated as functions of reduced electric field ( $E/n$ ) based on the solution of the Boltzmann equation, which is facilitated using the commercial software, BOLSIG+ [25]. Such an approach is necessary since the reactions are coupled to the electron energy distribution function. It is noteworthy that only elastic and inelastic cross sections associated with the major species  $N_2$  [26],  $O_2$  [27],  $CH_4$ ,  $H_2O$ , and  $CO_2$  [28] are considered in establishing the electron energy distribution. The species conservation equation solved has the form:

$$\frac{\partial n_j}{\partial t} = \sum_{\text{reactions}} (v_j' - v_j) \left[ k_f (E/n_{\text{tot}} \text{ or } T_e \text{ or } T_{\text{gas}}) \prod_i n_i^{v_i} - k_b \prod_i n_i^{v_i'} \right] - \nabla \cdot (n_j V_{D,j}) - V_{adv}^* \frac{\partial n_j}{\partial z} \quad (1)$$

with

$$\sum_i v_i n_{\text{reac},i} \xrightleftharpoons[k_b]{k_f} \sum_i v_i' n_{\text{prod},i} \quad (2)$$

The species equation is solved simultaneously with the energy equation:

$$\frac{\partial T_{\text{gas}}}{\partial t} = \frac{1}{\sum_{\text{species } j} c_{v,j} n_j} \left[ e n_e \mu_e E^2 + \sum_{\text{species } j} \left\{ -\frac{\partial (h_{f,j} n_j)}{\partial t} - \nabla \cdot (h_{\text{sens},j} n_j V_{D,j}) - V_{adv}^* \frac{\partial (h_{\text{sens},j} n_j)}{\partial z} \right\} + \nabla \cdot (\lambda \nabla T_{\text{gas}}) \right] \quad (3)$$

to compute the species number densities and gas temperature at each grid point. The species diffusion velocity  $V_{D,j}$  is composed of the diffusion-induced convection velocity  $V_c$ , the ordinary diffusion velocity, and the thermal diffusion velocity, the latter of which is accounted for light species only, having molecular weight less than five:

$$V_{D,j} = V_c - D_{jm} \frac{\nabla X_j}{X_j} + \frac{D_{jm} \Theta_{jm}}{X_j} \frac{\nabla T_{\text{gas}}}{T_{\text{gas}}} \quad (4)$$

Here  $V_c$  is determined to satisfy the condition:

$$\nabla \cdot \left( \sum_{\text{species } j} n_j V_{D,j} \right) = 0 \quad (5)$$

In the above equations,  $n_j$ ,  $X_j$  and  $v_j$  are the number density, mole fraction, and stoichiometric coefficient of species  $j$ ,  $k_f$  and  $k_b$  are the forward and reverse rate coefficients,  $T_e$  and  $T_{\text{gas}}$  are the electron and gas temperatures,  $D_{jm}$  is the mixture average diffusion coefficient of species  $j$ ,  $\Theta_{jm}$  is the thermal diffusion ratio of species  $j$ , and  $V_{adv}^*$  is the local advection velocity, which is scaled as  $T_{\text{gas}}/T_{\text{gas},i}$  ( $T_{\text{gas},i}$  is the initial inlet gas temperature) assuming negligible radial velocity and constant pressure, to account for the flow acceleration caused by heat release during combustion. We assume that electrons and ions exist only in the discharge region, and that the binary diffusion coefficients for electronically excited  $N_2$  are equal to those of the ground state  $N_2$ . In the energy equation,  $\mu_e$  is the electron mobility (a function of  $E/n$ ),  $c_{v,j}$  is the heat capacities at constant volume of species  $j$ ,  $h_{f,j}$  and  $h_{\text{sens},j}$  are the formation and sensible enthalpies of species  $j$ , and  $\lambda$  is the mixture-averaged thermal conductivity. The mixture diffusion coefficient of species  $j$ , thermal diffusion ratio of species  $j$ , and mixture-averaged thermal conductivity are computed at each grid points according to Eq. (6) (Bird et al., 1960), Eq. (7), and Eq. (8) (Mathur et al., 1967), i.e.,

$$D_{jm} = \frac{1 - Y_j}{\sum_{k \neq j} X_k / D_{kj}} \quad (6)$$

$$\Theta_j = \sum_{k \neq j} \theta_{jk} \quad (7)$$

$$\lambda = \frac{1}{2} \left( \sum_j X_j \lambda_j + \frac{1}{\sum_j X_j / \lambda_j} \right) \quad (8)$$

where  $X_j$  and  $Y_j$  are the mole and mass fractions of species  $j$ , respectively,  $D_{kj}$  is the binary diffusion coefficient between species  $k$  and  $j$ ,  $\theta_{jk}$  is the binary thermal diffusion ratio for species  $j$  into species  $k$ , and  $\lambda_j$  is the pure thermal conductivity of species  $j$ .

In solving the system of partial differential equations, the diffusion processes (species and thermal conduction) are discretized by a central difference scheme, and the convection and advection processes (species and enthalpy) are discretized by an upwind scheme. The system of ordinary differential equations is then solved implicitly for each (adaptive) time step based on a backward difference formula (BDF). In the computations, the domain

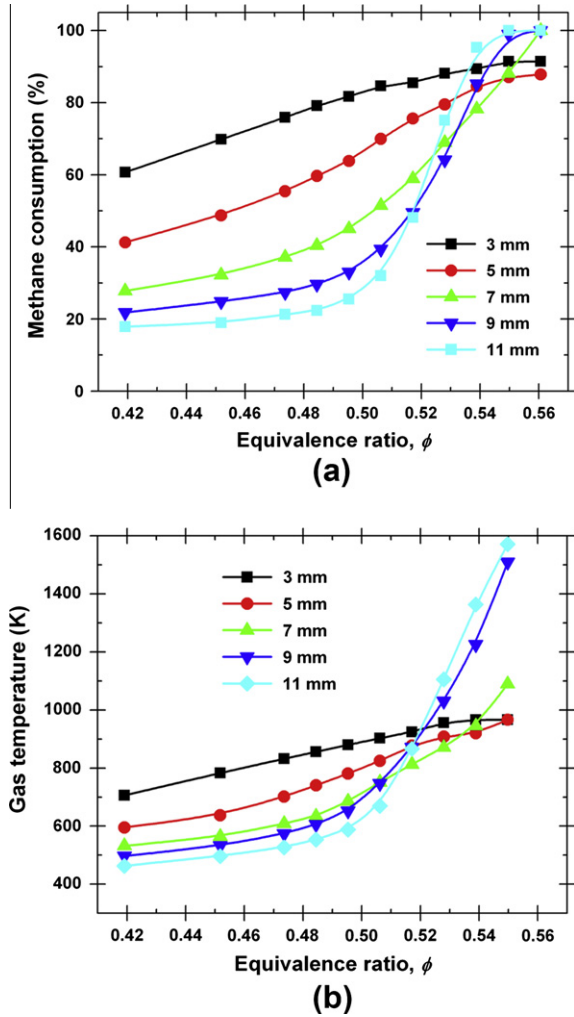


Fig. 3. (a) Methane consumptions and (b) gas temperatures measured between 3 and 11 mm at flow downstream location from the discharge operated at 30 kHz repetition rate.

is divided into smaller subdomains, which are allocated to separate processes. These processes are computed in parallel, synchronizing their boundary values via the message passing interface, MPI. *Sundials CVODE* with MPI support [29] is used as a solver and Open MPI [30] is used for MPI-2 standard implementation. Each temporal solution is computed iteratively using the Generalized Minimal Residual method (*GMRES*) [31]. A Dirichlet condition is used for the lower domain boundary, whereas Neumann conditions are used for the sides and top of the computational boundary.

A Gaussian-shaped (temporally) reduced electric field with 9 ns half maximum pulse width is applied at the discharge region in accordance with the voltage pulse characterized in the experiments. The peak reduced electric field used in the simulation is determined to be 328 Td for methane/air at  $\phi = 0.45$  and 330 Td for  $\phi = 0.55$  by matching the measured gas temperature to the simulated temperature (this comparison is shown later). The initial inlet gas temperature and pressure are set to 296 K and 1 atm, respectively.

#### 4. Gas chromatographic and temperature results

The percentage in the extent of methane consumption (or local combustion efficiency)  $\eta$  is defined as:

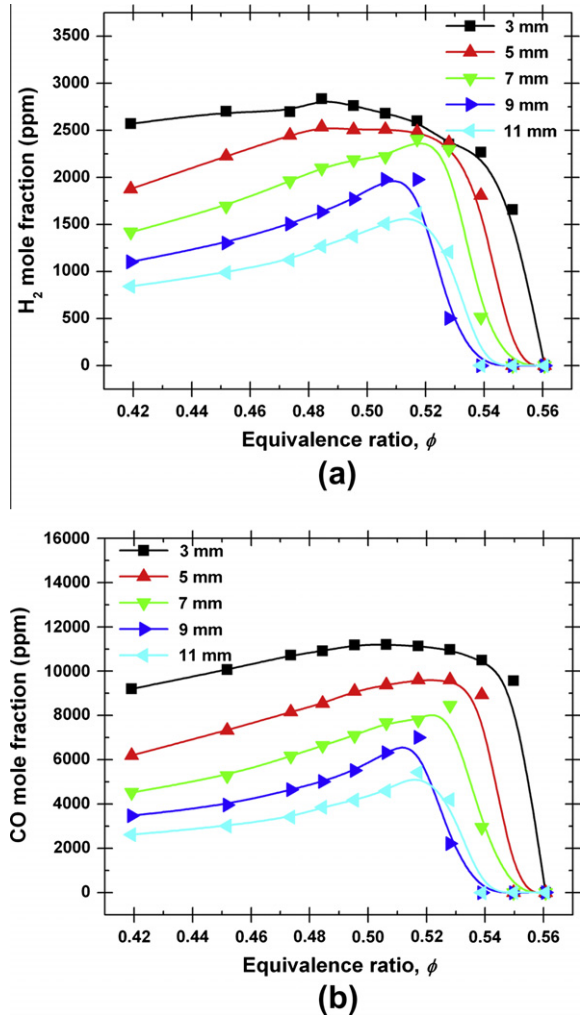


Fig. 4. (a) H<sub>2</sub> and (b) CO concentrations measured between 3 and 11 mm at flow downstream location from the discharge operated at 30 kHz repetition rate.

$$\eta = \frac{X_{\text{methane},i} - X_{\text{methane}}}{X_{\text{methane},i}} \times 100 \quad (9)$$

where  $X_{\text{methane},i}$  and  $X_{\text{methane}}$  are the initial and local methane mole fractions, respectively.

#### 4.1. Measurements made along the flow direction downstream of the discharge

Measurements of the extent of methane consumption (Fig. 3a) and gas temperature (Fig. 3b) are made along the axis centered about the discharge between 3 and 11 mm downstream of the discharge. For these measurements, the discharge is operated at 30 kHz repetition rate. No combustion is achieved without the use of the discharge. Methane consumption is moderately high (60–90%) at 3 mm downstream for equivalence ratios between 0.42 and 0.56. When the equivalence ratio is above 0.54, combustion appears to be complete. However, when the equivalence ratio is below 0.54, the extent of combustion decreases precipitously with increased height above the discharge due to mixing with the surrounding unburnt premixed methane/air mixture. A similar trend is seen in the measured gas temperatures. The gas temperature is moderately high (700–950 K) at a location of 3 mm downstream of the discharge over the range of equivalence ratios. However, at equivalence ratios below 0.54, it decreases strongly

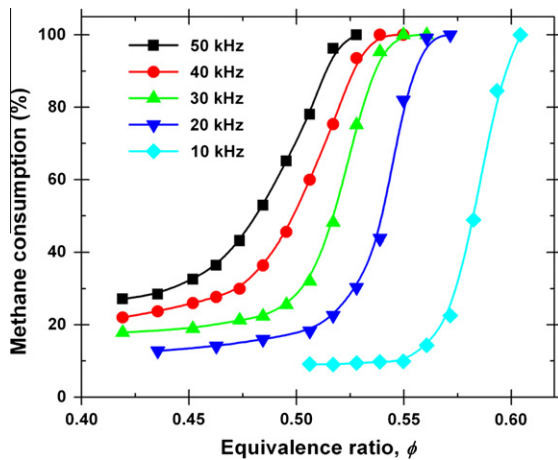


Fig. 5. Methane consumption measured at 11 mm flow downstream from discharges as functions of equivalence ratio for 10 kHz, 20 kHz, 30 kHz, 40 kHz, and 50 kHz discharge repetition rates.

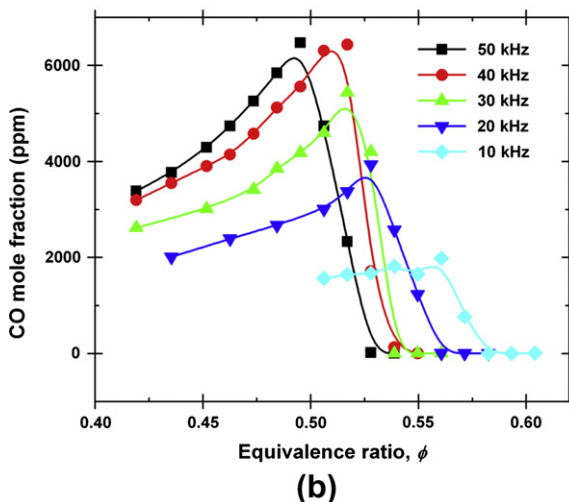
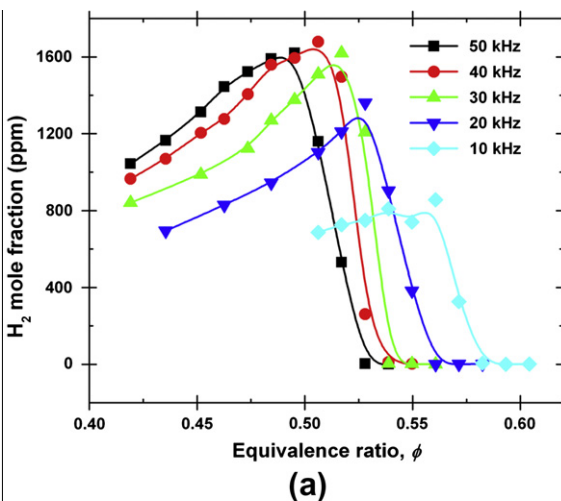


Fig. 6. (a) H<sub>2</sub> and (b) CO concentrations measured at 11 mm flow downstream location from the discharge at discharge repetition rates between 10 kHz and 50 kHz.

with increasing distance above the discharge. Above an equivalence ratio of 0.54 it rises close to the laminar flame temperature

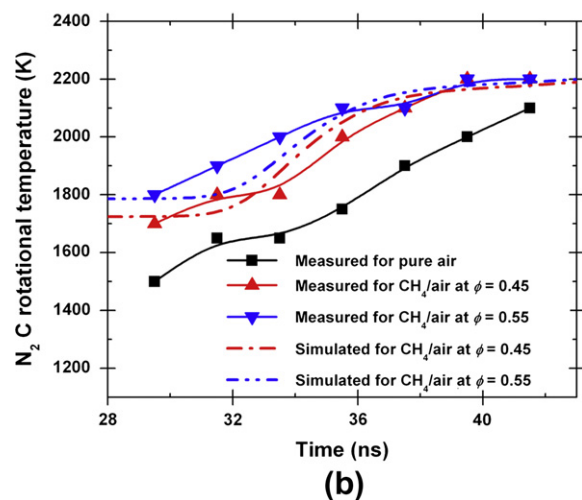
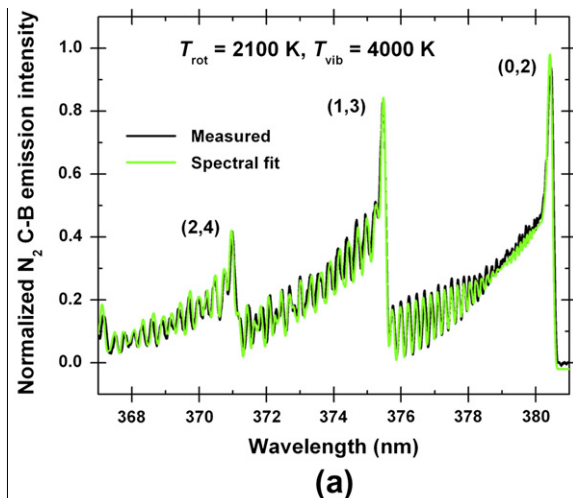
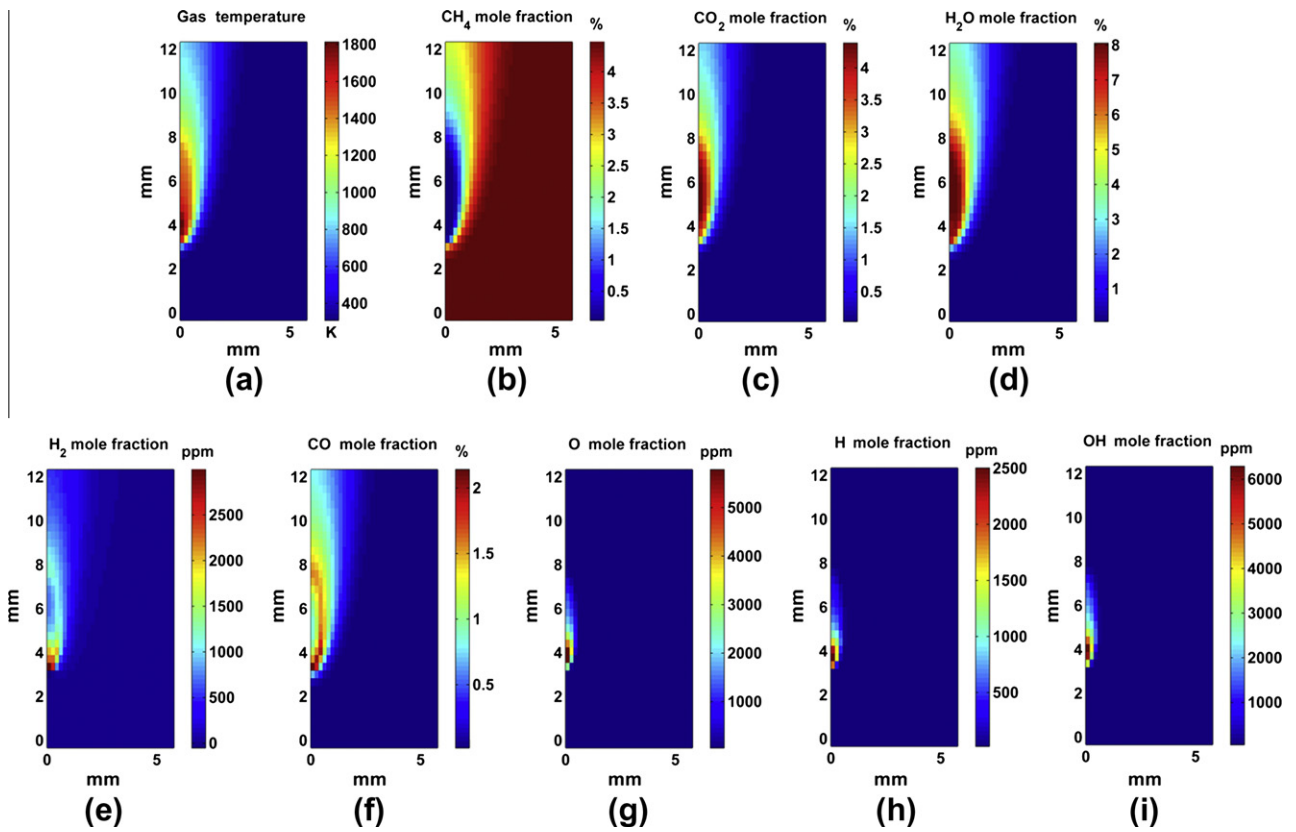


Fig. 7. (a) Example of measured emission spectrum of N<sub>2</sub> C-B (0,2), (1,3), (2,4) bands with its spectral fit and (b) temporal evolutions of rotational temperature for pure air and methane/air mixtures at  $\phi = 0.45$  and 0.55, as well as those obtained from 2-D kinetic simulations conducted at  $\phi = 0.45$  and 0.55.

with increased distance from the discharge. Interestingly, this threshold equivalence ratio, 0.54, is very close to the known (undiluted zero stretch) lean flammability limit of methane/air mixtures ( $\phi = 0.53$  [32]). These results suggest that the extension in the lean flammability limit is not significant, and is instead highly localized with incomplete combustion.

H<sub>2</sub> and CO concentrations are also measured along the flow direction downstream of the discharge. These measurements are shown in Fig. 4a and b, respectively. When the equivalence ratio is well below 0.54, H<sub>2</sub> and CO concentrations are superequilibrium, i.e., higher than those calculated for the thermally equilibrated state and they tend to decrease with downstream distance due to the mixing with the surrounding unburnt mixture. However, when the equivalence ratio is above 0.54, these intermediate species are rapidly consumed in the ensuing flame, and little or no H<sub>2</sub> and CO is detected downstream of the discharge. We note that the oxidation of CO, which results in a significant portion of the heat release of combustion, has a relatively high threshold temperature (about 1500 K), therefore, it is expected that CO will persist downstream of the discharge at the relative cool stream temperature when the equivalence ratio is below 0.54. At  $\phi = 0.53$ , H<sub>2</sub> and CO concentrations increase between 9 mm and 11 mm downstream locations. This increase is a result of an extension of the location



**Fig. 8.** Simulated spatial distributions of (a) gas temperature and (b) CH<sub>4</sub>, (c) CO<sub>2</sub>, (d) H<sub>2</sub>O, (e) H<sub>2</sub>, (f) CO, (g) O, (h) H, and (i) OH mole fractions when the flow speed is 42.5 cm/s, the discharge repetition rate is 30 kHz, and methane/air mixture is at  $\phi = 0.45$ .

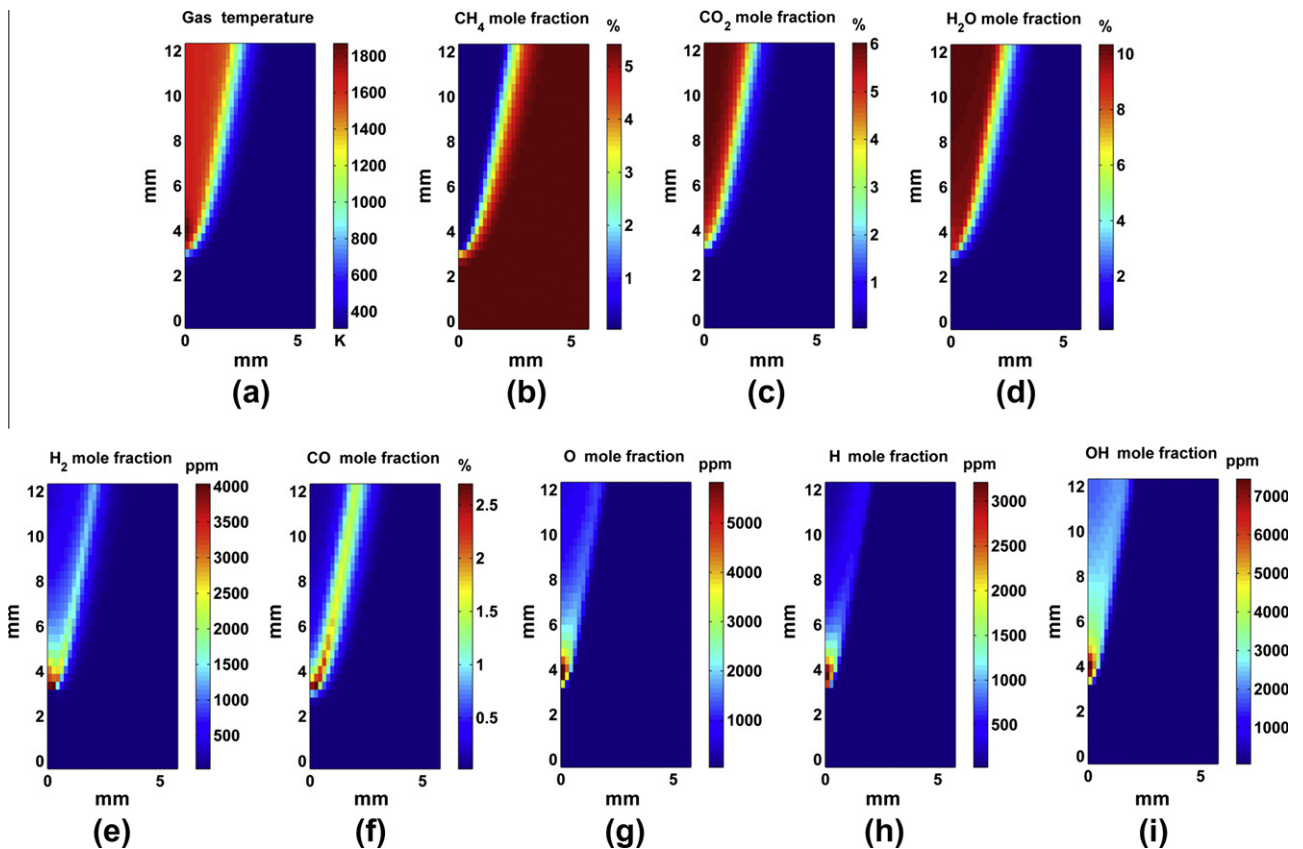


**Fig. 9.** Simulated spatial distributions of (a) gas temperature and (b) CH<sub>4</sub>, (c) CO<sub>2</sub>, (d) H<sub>2</sub>O, (e) H<sub>2</sub>, (f) CO, (g) O, (h) H, and (i) OH mole fractions when the flow speed is 42.5 cm/s, the discharge repetition rate is 30 kHz, and methane/air mixture is at  $\phi = 0.55$ .

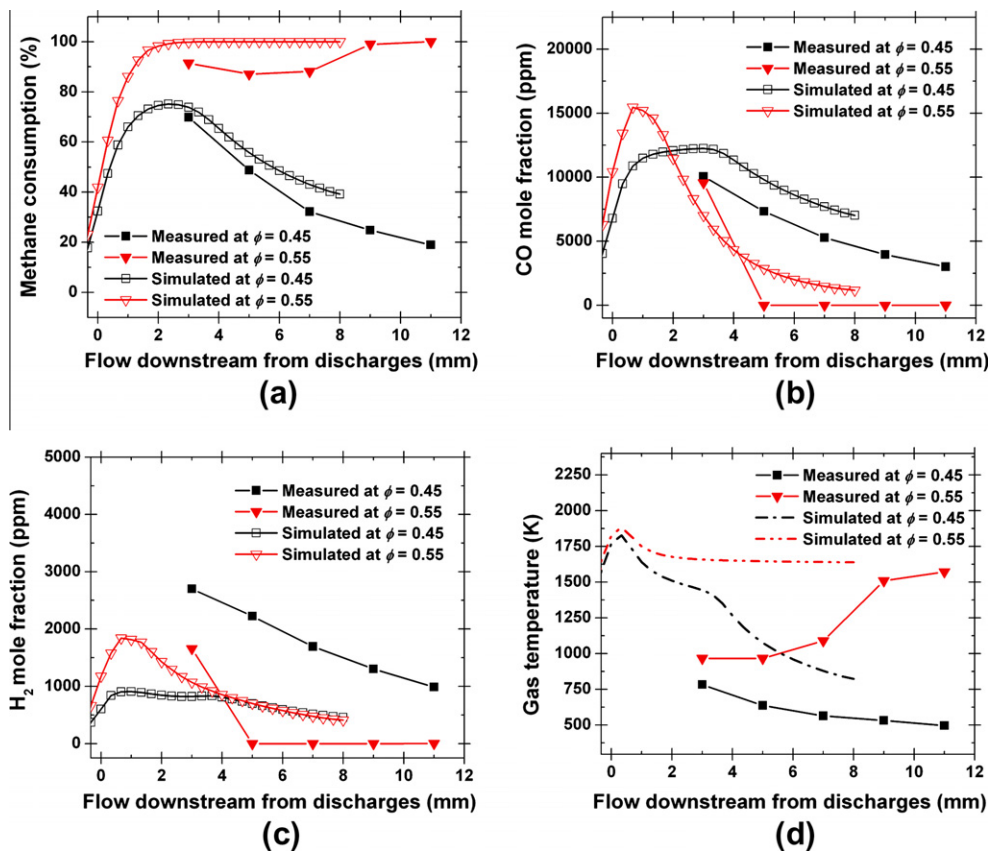


Fig. 10. Comparison of (a) methane consumption ( $\eta$ ), (b) CO, (c) H<sub>2</sub> mole fractions and (d) gas temperature along discharge downstream locations between the simulation and the experimental results for methane/air at  $\phi = 0.45$  and 0.55.

where quenching of the combustion is taking place. H<sub>2</sub> and CO concentrations are lower upstream of these locations because of their consumption as a result of the plasma-assisted combustion.

#### 4.2. Measurements made at different discharge repetition rates

To determine if the discharge repetition rate has an effect on the extension of the lean flammability limit, sampling is carried out at a fixed downstream location of 11 mm while varying the equivalence ratio over a range of discharge repetition rates between 10 kHz and 50 kHz. The resulting measurements of methane consumption are shown in Fig. 5. We see that higher repetition rates favor increased methane consumption for any given equivalence ratio. We also confirm that consumption increases with increasing equivalence ratio from 0.42 to 0.605 for all tested repetition rates. The equivalence ratio for complete combustion (as measured to within an experimental error of about 2%) decreases substantially with increasing repetition rate. However, we note that for the highest rate studied (50 kHz), the limit for complete combustion was still only  $\phi = 0.53$ , lying just on the often quoted value for the lean flammability limit of about 0.53. While consumption (partial combustion) does take place below this limit, it is clear from Fig. 5, that it is relatively incomplete over the range of discharge frequencies examined here.

H<sub>2</sub> and CO concentrations are measured at the fixed downstream location of the discharge while varying discharge repetition rates between 10 kHz and 50 kHz. The results are shown in Fig. 6a and b, respectively. These species are found to be completely consumed for all tested frequencies as equivalence ratios reach values slightly below the corresponding lean flammability limits. This confirms that the depletion of these intermediates above the lean

flammability limit results from downstream propagation of the combustion process. On the other hand, the higher repetition rate provides higher concentrations in these intermediates (H<sub>2</sub> and CO) when the equivalence ratio is below the limit.

#### 5. Spectroscopic emission results

Time-resolved N<sub>2</sub> C–B emission spectra are recorded to obtain the rotational and vibrational temperatures of the discharge. Figure 7a shows an example of spectrum (black) measured for methane/air at  $\phi = 0.55$  at the time when the emission intensity is highest and its spectral fit (green) synthesized with  $T_{rot} = 2100$  K and  $T_{vib} = 4000$  K assuming that the energy state populations follow Boltzmann distributions. Their temporal evolutions in pure air and methane/air at  $\phi = 0.45$  and 0.55 are shown in Fig. 7b. The rotational temperature increases extremely fast (35 K/ns) during the pulse duration while the vibrational temperature (not shown) is kept at 4000 K. Since the rotational–translation (R–T) relaxation time is shorter than the pulse duration at this (high) pressure, this fast gas temperature increase is mostly due to collisional quenching of electronically excited species produced by electron-impacts. The initial gas temperature is found to be initially elevated due to the repetitive pulses and increases with increasing  $\phi$  because a higher  $\phi$  is generally associated with greater heat release. However, a greater portion of the energy that results in gas heating originates from the discharge through Ohmic dissipation rather than from the combustion process in the conditions examined here. Meanwhile, the peak  $E/ns$  used in the simulations are determined by matching the rises of the measured rotational and simulated gas temperatures. The simulated gas temperatures for methane/air at  $\phi = 0.45$  and 0.55 are also shown in Fig. 7b.

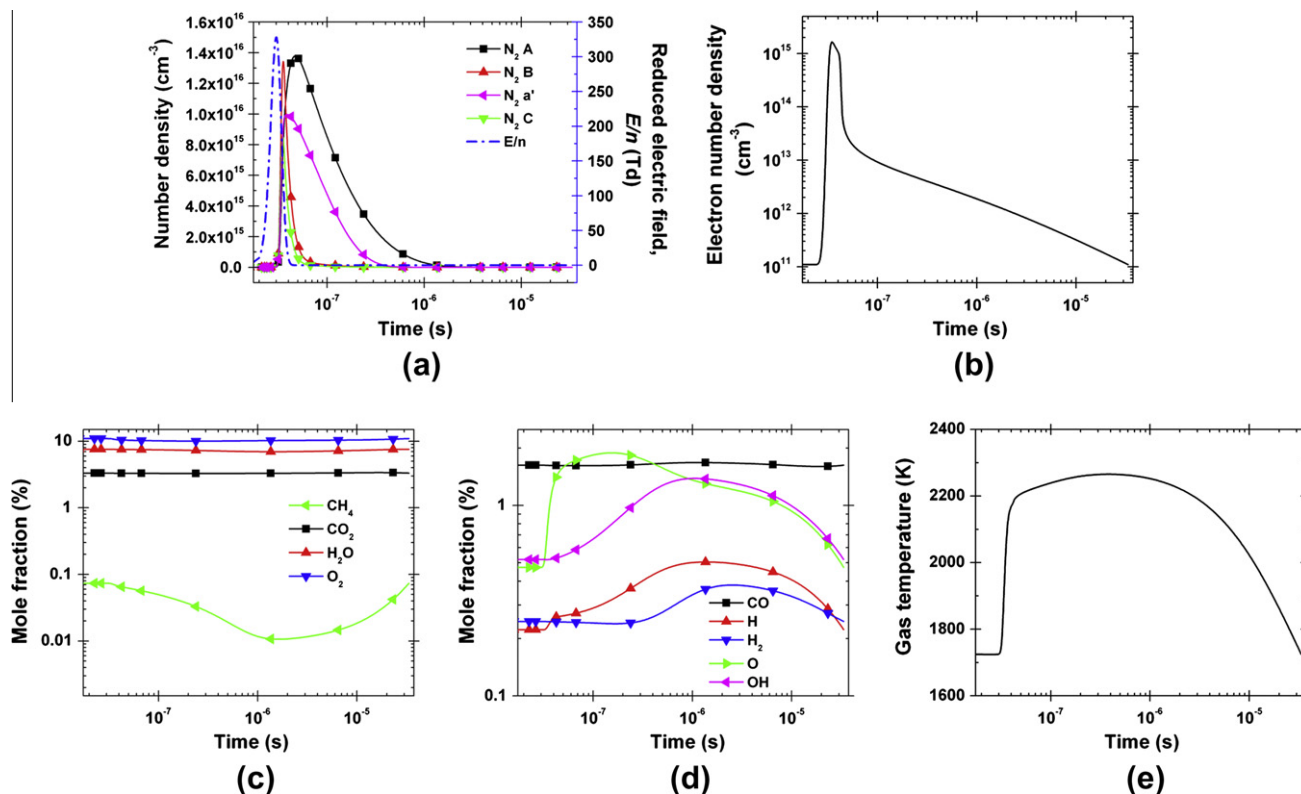


**Fig. 11.** Simulated temporal evolutions of (a) excited electronic states of  $N_2$  number densities, (b) electron number density, (c)  $CH_4$ ,  $O_2$ ,  $CO_2$ , and  $H_2O$  mole fractions, (d)  $CO$ ,  $H$ ,  $H_2$ ,  $O$ , and  $OH$  mole fractions, and (e) gas temperature within the discharge during a single period when the flow speed is 42.5 cm/s, the discharge repetition rate is 30 kHz, and a methane/air is at  $\phi = 0.45$ .

## 6. Simulation results

The 2-D kinetic simulations are conducted for methane/air mixtures at  $\phi = 0.45$  and 0.55 corresponding to values below and above lean flammability limits. The flow speed and discharge repetition rate are 42.5 cm/s and 30 kHz in accordance with the experiments. The computation advances until properties (species mole fractions and gas temperature) reach quasi steady state values.

### 6.1. Simulation results for methane/air mixture at $\phi = 0.45$

The spatial distributions of gas temperature and  $CH_4$ ,  $CO_2$ ,  $H_2O$ ,  $H_2$ ,  $CO$ ,  $O$ ,  $H$ , and  $OH$  mole fractions for a methane/air mixture at  $\phi = 0.45$  are shown in Figs. 8a–i, respectively. Complete combustion is achieved within the discharge region, but this extends only to the immediate post-discharge region. In this region the  $CH_4$  is consumed and converted to  $CO_2$  and  $H_2O$ . The radicals ( $O$ ,  $H$ , and  $OH$ ), key species in the combustion process, participating branching/propagation reactions are present in this region in significant amounts. However, the combustion process is seen to be quenched as a result of mixing with the less-reactive and cooler surroundings. Reactions involving radicals are terminated and the partial oxidation products ( $H_2$  and  $CO$ ) begin to appear outside of the immediate discharge region. The flow is further diluted by both diffusion and advection at the distant downstream locations. The gas temperature is high (1724 K) within the discharge region due to the discharge energy addition and heat of combustion but decreases precipitously with downstream position.

### 6.2. Simulation results for methane/air mixture at $\phi = 0.55$

The spatial distributions of gas temperature and  $CH_4$ ,  $CO_2$ ,  $H_2O$ ,  $H_2$ ,  $CO$ ,  $O$ ,  $H$ , and  $OH$  mole fractions for a methane/air mixture at

$\phi = 0.55$  are shown in Figs. 9a–i, respectively. At this equivalence ratio, the combustion induced by the discharge is seen to propagate radially at downstream locations, establishing a thin radially-spanning self-sustained reaction zone (flame front). The  $CH_4$  is found to be entirely converted into  $CO_2$  and  $H_2O$  behind the flame, raising the temperature to about 1600 K, close to the adiabatic flame temperature of 1577 K. The intermediate species ( $H_2$  and  $CO$ ) exist in significant amounts only within the flame region, with radicals existing within the flame and the post-flame region as a result of the high post-flame temperature. The gas temperature, as well as intermediate species and radical mole fractions are highest within the discharge, as expected, reaching quasi steady state temperatures of 1786 K.

### 6.3. Comparison between the simulation and experimental results

Comparisons are made between the results of our simulation and experimental measurements of methane consumption ( $\eta$ ),  $H_2$ ,  $CO$  mole fractions, and gas temperature. In calculating simulated mole fractions, species number densities are integrated over the sampling probe area to account for the finite diameter of the probe. These comparisons are shown in Fig. 10a–d, respectively. The predicted quenching of the combustion process at downstream locations when  $\phi = 0.45$ , and the sustained combustion when  $\phi = 0.55$ , agree well with the simulation results, as determined by the predicted and measured methane consumption,  $\eta$  (Fig. 10a). We attribute the slightly lower measured  $\eta$  to the non-zero radial flow velocity and weak quenching of combustion by the intrusion of the sampling probe. For  $CO$  and  $H_2$ , the simulated values are correspondingly slightly higher and lower than the measurements respectively when  $\phi = 0.45$ . At  $\phi = 0.55$ , the measured  $CO$  and  $H_2$  mole fractions are comparable to those predicted at a downstream sampling location of 4 mm, but both seem

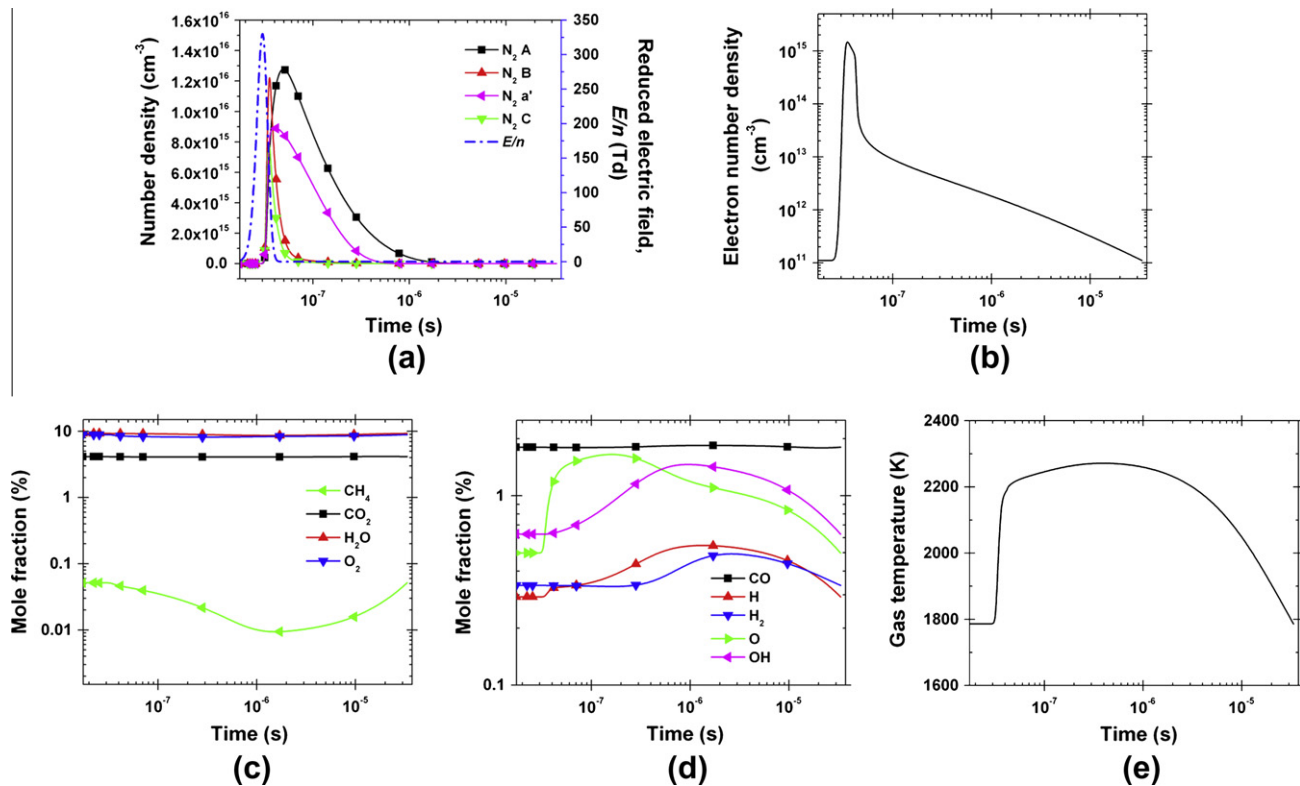


**Fig. 12.** Simulated temporal evolutions of (a) excited electronic states of  $N_2$  number densities, (b) electron number density, (c)  $CH_4$ ,  $CO_2$ ,  $H_2O$ , and  $O_2$  mole fractions, (d)  $CO$ ,  $H$ ,  $H_2$ ,  $O$ , and  $OH$  mole fractions, and (e) gas temperature within the discharge during a single period when the flow speed is 42.5 cm/s, the discharge repetition rate is 30 kHz, and a methane/air is at  $\phi = 0.55$ .

to be below the predicted amounts at farther downstream locations. We attribute this to reactions that continue to occur within the sampling probe. Also, discrepancies are seen between the simulated and measured gas temperature close to the discharge. We believe that this is due to the intrusive nature of the thermocouple probe, likely resulting in a strong quenching of combustion process, particularly in that region close to the discharge where the combusting volume is relatively small.

#### 6.4. Kinetics at the discharge region

The temporal variation in the number densities of excited electronic states of  $N_2$ , and electrons, as well as the mole fractions of major combustion species ( $CH_4$ ,  $O_2$ ,  $CO_2$ , and  $H_2O$ ), minor combustion species ( $CO$ ,  $H$ ,  $H_2$ ,  $O$ , and  $OH$ ), and gas temperature within the discharge during a single period for methane/air at  $\phi = 0.45$  are shown in Figs. 11a–e, respectively. A relatively low methane mole fraction persists over the entire time between pulses (Fig. 11c), since species diffusion/advection is much slower than the reaction time scale, and there is insufficient time for methane to diffuse into the reaction zone between pulses, from the surrounding unburnt mixture. The electron number density peaks during the discharge (Fig. 11b) at a value of about  $1.6 \times 10^{15} \text{ cm}^{-3}$ , from an initial value of about  $1.1 \times 10^{11} \text{ cm}^{-3}$ . These electrons, strongly energized by the pulsed electric field, produce electronically excited species, i.e.,  $N_2$  (A, B, a', C), as seen in Fig. 11a. These excited species are then quenched via collisions, mainly with  $N_2$  and  $O_2$ , because of the fuel-lean conditions of this study. Since these excited state energies exceed that to dissociate  $O_2$ , a significant amount of O atoms are produced (up to 1.9% in mole fraction) as a result of dissociative quenching, and the excess energy is released as energetic O atoms which subsequently thermalize and rapidly heat the gas.

The generated atomic oxygen are also involved in reactions to form intermediates such as OH, H, and  $H_2$ . The mole fractions of these active species, peaking in time well after the peak in electron number density,  $N_2$  excited state densities, and O atom density, are relatively high, and they diffuse out beyond the discharge region into the surrounding flow. The gas temperature, which rises rapidly during the pulse, also decreases as a result of heat diffusion/advection.

The same temporal variations of properties within the discharge as those of Fig. 11, for the case of  $\phi = 0.55$ , are shown in Fig. 12. The differences are minor, with only slight differences in the species mole fractions, and the exception that initial gas temperature is elevated because of the increased equivalence ratio,  $\phi$ .

## 7. Conclusions

We investigated the structure of nanosecond repetitive pulsed discharge enhancement of laminar premixed methane/air combustion near the lean flammability limit. Experiments characterized the species mole fractions and temperature at locations downstream of the discharge. For equivalence ratios,  $\phi = 0.45$ , less than that associated with the lean flammability limit, the nonequilibrium plasma was able to sustain ignition of the flow, but the extent of combustion was seen to diminish with downstream position. At an equivalence ratio  $\phi = 0.55$ , just above the lean limit, the combustion propagated beyond the discharge into the surrounding flow. 2-D kinetic simulations revealed that the discharge produces a significant amount of active species (O, H, OH,  $H_2$  and CO) and heat indirectly through dissociative quenching of nitrogen by molecular oxygen following the production of electronically excited  $N_2$  states via electron-impact. The localized discharge was found to serve as a source of radicals and heat, which diffuse out

into the surrounding flow serving as a flame-holder, sustaining combustion under otherwise adverse conditions.

## Acknowledgments

This work is supported by the National Science Foundation and the Department of Energy through the NSF/DOE Partnership in Basic Plasma Science.

## References

- [1] G. Pilla, D. Galley, D.A. Lacoste, F. Lacas, D. Veynante, C.O. Laux, *IEEE Trans. Plasma Sci.* 34 (2006) 2471–2477.
- [2] A. Bao, Y.G. Utkin, S. Keshav, G. Lou, I.V. Adamovich, *IEEE Trans. Plasma Sci.* 35 (2007) 1628–1638.
- [3] L. Wu, J. Lane, N.P. Cernansky, D.L. Miller, A.A. Fridman, A.Y. Starikovskii, *Proc. Combust. Inst.* 33 (2011) 3219–3224.
- [4] S.V. Pancheshnyi, D.A. Lacoste, A. Bourdon, C.O. Laux, *IEEE Trans. Plasma Sci.* 34 (2006) 2478–2487.
- [5] W. Kim, M.G. Mungal, M.A. Cappelli, *Combust. Flame* 157 (2009) 374–383.
- [6] A.A. Nikipelov, I.B. Popov, G. Correale, A.E. Rakitin, A.Y. Starikovskii, in: 48th AIAA Aerospace Science Meeting including the New Horizons Forum and Aerospace Exposition, Orlando, Florida, 2010.
- [7] M.S. Bak, W. Kim, M.A. Cappelli, *Appl. Phys. Lett.* 98 (2011) 011502.
- [8] M. Uddi, N. Jiang, I.V. Adamovich, W.R. Lempert, *J. Phys. D* 42 (2009) 075205.
- [9] N.L. Aleksandrov, S.V. Kindysheva, E.N. Kukaev, S.M. Starikovskaya, A.Y. Starikovskii, *Plasma Phys. Rep.* 35 (2009) 867–882.
- [10] D.Z. Pai, D.A. Lacoste, C.O. Laux, *J. Appl. Phys.* 107 (2010) 093303.
- [11] W.E. Kaskan, *Proc. Combust. Inst.* 6 (1957) 134–143.
- [12] A. Kazakov, M. Frenklach. <<http://www.me.berkeley.edu/drm/>>.
- [13] M. Frenklach, H. Wang, C.-L. Yu, M. Goldenberg, C.T. Bowman, R.K. Hanson, D.F. Davidson, E.J. Chang, G.P. Smith, D.M. Golden, W.C. Gardiner, V. Lissianski. <[http://www.me.berkeley.edu/gri\\_mech/](http://www.me.berkeley.edu/gri_mech/)>.
- [14] A. Burcat, Third Millennium Ideal Gas and Condensed Phase Thermochemical Database for Combustion, Technion-Israel Institute of Technology, TAE 867, 2001.
- [15] M. Capitelli, C.M. Ferreira, B.F. Gordiets, A.I. Osipov, *Plasma Kinetics in Atmospheric Gases*, Springer, Berlin, Germany, 2000.
- [16] I.A. Kossyi, A.Y. Kostinsky, A.A. Matveyev, V.P. Silakov, *Plasma Sources Sci. Technol.* 1 (1992) 207–220.
- [17] C.H. Sheehan, J.-P. St.-Maurice, *Adv. Space Res.* 33 (2004) 216–220.
- [18] S. Rosen, A. Derkatch, J. Semaniak, A. Neau, A. Al-Khalili, A. Le Padellec, L. Viktor, R. Thomas, H. Danared, M. af Ugglas, M. Larsson, *Faraday Discuss.* 115 (2000) 295–302.
- [19] N.L. Aleksandrov, S.V. Kindysheva, A.A. Kirpichnikov, I.N. Kosarev, S.M. Starikovskaia, A.Y. Starikovskii, *J. Phys. D* 40 (2007) 4493–4502.
- [20] J.C. Person, D.O. Ham, *Radiat. Phys. Chem.* 31 (1988) 1–8.
- [21] M.F. Golde, G.H. Ho, W. Tao, J.M. Thomas, *J. Phys. Chem.* 93 (1989) 1112–1118.
- [22] L.G. Piper, *J. Chem. Phys.* 97 (1992) 270–275.
- [23] H. Umamoto, R. Ozeki, M. Ueda, M. Oku, *J. Chem. Phys.* 86 (2002) 6885–6892.
- [24] F. Albugues, A. Birot, D. Blanc, H. Brunet, J. Galy, P. Millet, J.L. Teyssier, *J. Chem. Phys.* 61 (1974) 2695–2699.
- [25] G.J.M. Hagelaar, L.C. Pitchford, *Plasma Sources Sci. Technol.* 14 (2005) 722–733.
- [26] A.V. Phelps, L.C. Pitchford Database. <<http://www.lxcat.laplace.univ-tlse.fr>> (retrieved 16.02.11).
- [27] A.V. Phelps Database. <<http://www.lxcat.laplace.univ-tlse.fr>> (retrieved 16.02.11).
- [28] M. Hayashi Database. <<http://www.lxcat.laplace.univ-tlse.fr>> (retrieved 16.02.11).
- [29] A.C. Hindmarsh, P.N. Brown, K.E. Grant, S.L. Lee, R. Serban, D.E. Shumaker, C.S. Woodward, *ACM Trans. Math. Softw.* 31 (2005) 363–396.
- [30] <http://www.open-mpi.org/>.
- [31] Y. Saad, M.H. Schultz, *SIAM J. Sci. Comput.* 7 (1986) 856–869.
- [32] H.F. Coward, G.W. Jones, US Bureau of Mines, Bulletin 503, 1952.